JOURNAL OF PROPULSION AND POWER
Vol. 21, No. 3, May–June 2005

Direct Numerical Simulation of Solid Propellant Combustion in Crossflow

Brian A. McDonald*
Stone Engineering Company, Huntsville, Alabama 35805
and
Suresh Menon†
Georgia Institute of Technology, Atlanta, Georgia 30332

A direct numerical simulation (DNS) of a homogeneous ammonium perchlorate/hydroxyl-terminated polybutadiene solid propellant in crossflow was carried out to provide proper boundary conditions to an interior ballistics model. A two-step global finite-rate chemistry model for ammonium perchlorate decomposition and decomposition gas–binder gas reactions was used. An Arrhenius pyrolysis model was used to describe the propellant regression rate. Using strand burn rate data, the DNS model was calibrated by modeling an environment with no crossflow and adjusting thermodynamic properties in the gas/solid to match the measured regression rate. Crossflow Mach numbers were then induced, ranging from $M = 0.0$ to 0.8, where the calculated regression rates are compared to the base regression rate at $M = 0.0$. The analysis shows that near-wall vorticity increases with Mach number, but does not significantly reduce the flame to wall stand-off distance. Temperature gradients due to boundary layer compression are shown to dominate the regression rate. The validity of the results was tested by incorporating them into an interior ballistics model to simulate the performance of an actual rocket motor and compare to static test data. A simplified DNS heat-transfer-based analysis is presented and shown to produce similar conclusions.

I. Introduction

THE development of erosive burning models for interior ballistics purposes dates back to the 1950s. The primary purpose of these models is to better predict or simulate rocket motor chamber pressure and performance in motors with erosive burning. In most design phases of solid rocket motors (SRMs), subscale burn-rate data, either from strand data or from standard 2×4 in. motors, are all that is available. The burn-rate behavior of a given propellant in crossflow is usually unknown. Strand data are typically collected in a closed bomb[1] or standard 2×4 in. motor. The bombs are prepressurized with an inert gas to a selected pressure and provide a convenient means of characterizing a propellant's burn rate versus pressure. However, the environment is relatively stagnant and provides no means for inducing a crossflow at the burning surface. Many small SRMs have high propellant volumetric loading fractions for weight efficiency. For these motors, the internal flow Mach numbers (M) can approach unity; thus, significant crossflow velocities at the propellant surface can be induced.

As the chamber M increases, the resulting crossflow velocity at the propellant surface results in heat transfer conditions that deviate considerably from the condition in the strand burner test. The burn rate experienced at a local static pressure (P) condition in the full-scale motor is greater than the strand burner data at the same pressure and can be attributed to the increased heat transfer from the hot combustion gases in crossflow to the propellant.[2] This increase in burn rate, called erosive burning, can be seen clearly in full-scale motor tests as shown in Fig. 1.

The figure shows two curves, one being the measured data, and the other being a prediction using a three-dimensional internal ballistics code with the burning rate of the propellant calculated with the equation $r = cP^n$ calibrated to strand data, where c and n are the empirical rate coefficient and exponent, respectively. The measured pressure data show an extended pressure spike at the beginning of the trace, which is characteristic evidence of a strong influence of erosive burning (other more transient events include the igniter discharge and dynamic burning).

Erosive burning is defined as the increase in burning rate of a solid propellant that occurs as a function of hot gas crossflow at the propellant surface.[3] The amount of burning rate increase is established by comparing the erosive burning rate to the burning rate that occurs at the same local pressure for no crossflow. The primary mechanism for the increase in rate is the additional heat that is fluxed into the surface as a result of the crossflow. Several factors contribute to this increase in heat flux, including the thermal gradient in the boundary layer and turbulent enhancement of the local transport properties.

As the freestream flow velocity is increased over the burning propellant, the boundary layer is compressed. Thus, the temperature gradient at the surface of the propellant is increased which results in an increase in heat transfer to the surface. Although the pyrolysis of a composite propellant is complex in that several constituents outgas from the surface at different melt temperatures, the net activation energy of the pyrolysis process is very high; small changes in temperature result in large increases in pyrolysis rate. Thus, the pyrolysis process acts similarly to a simple melt process. The increase in energy flux to the surface is balanced by an increase in the pyrolysis rate, as opposed to a substantial increase in the surface layer temperature (the surface layer refers to a thin layer near the propellant surface composed mostly of decomposed ammonium perchlorate (AP) and binder gas).

The second mechanism that contributes to erosive burning is the increase in local transport properties due to turbulent fluctuations. The primary effect of turbulence is to increase the apparent thermal conductivity and thus increase the heat flux from the hot free stream combustion gases through the boundary layer to the surface. Apparent conductivity refers to the increase in heat transfer due to turbulent fluctuations. A secondary effect is an increase in the mixing rate of the decomposed AP (APd) and binder in the diffusion flame. As the boundary layer compresses, the near wall gas temperature increases which results in higher reaction rates.

Several analytical studies of erosive burning have been conducted. Razdan and Kuo[4] used a turbulent boundary layer approach to show

Received 12 April 2004; revision received 30 September 2004; accepted for publication 8 October 2004.

*Vice President/Technical Director; brianm@stoneeng.com. Member AIAA.

†Professor, Director, Computational Combustion Laboratory, School of Aerospace Engineering, 270 Ferst Drive; suresh.menon@aerospace.gatech.edu. Associate Fellow AIAA.

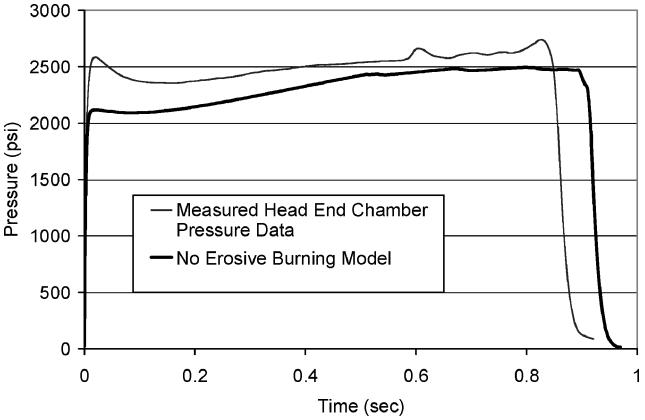

Fig. 1 CKEM measured chamber pressure.

that the augmented burning rate with freestream velocity is due to the increased heat feedback and increase in transport coefficients, as well as increased turbulent mixing. Gordon et al.[5] used a one-dimensional wall zone model coupled with a fully turbulent two-dimensional description of the whole flow field to develop an erosive burning model correlated to wall shear stress. They also concluded that the propellants' normal burning rate was the primary influence on the threshold for erosive burning. As the specific mass flow rate (mass flow per unit area) increases from the surface, the turbulent intensity increases. Bulgakov and Karpov[6] also used the boundary layer equations to study the burning of stick propellant and negative erosive burning (a decrease in burning rate with blowing across the surface) and found satisfactory agreement with experimental data. The decrease in burn rate was found to result from a decrease of heat flux into the surface as the flame zone moved away from the wall in developing flow. King[7] conducted a very extensive survey of experimental methods, as well as numerical techniques and correlations. He classified the most widely used models into three primary areas, including the following: 1) those based on augmented heat transfer from the core flow, 2) those based on alteration of transport properties in the region between the flame zone and the propellant surface, and 3) those based on chemically reacting boundary layers. He also developed a "second generation" model built on a zero-crossflow composite propellant burning model that includes two mechanisms for burning rate augmentation, the bending of a columnar diffusion flame by the crossflow and the mixing and heat transport augmentation by crossflow-induced turbulence. An eddy viscosity model was used for closure in the boundary layer analysis.

Most recently, Mukunda and Paul[8] conducted a study to examine the universal behavior of erosive burning. They completed a thorough review of the available data and correlations and concluded that for most practical propellants, erosive burning effects are primarily a function of the nonerosive mass flux and the Reynolds number, with little effect due to chemical kinetics. Apte and Yang[9] have used LES to study solid propellant combustion in crossflow and showed that turbulent mixing dominates over chemistry.

As the literature shows, the primary mechanism involved in erosive burning is the crossflow-augmented heat transfer from the flame front to the burning surface, changing the energy balance at the solid–gas interface. Direct numerical simulation (DNS) provides an accurate means of resolving all relevant scales in the erosive burning problem. This paper describes the results of using DNS to analyze the primary mechanisms which govern erosive burning. A high-rate AP and HTPB (hydroxyl-terminated polybutadiene) propellant that has considerable strand burn rate data and full-scale motor data available is chosen for the analysis. A two-step global finite-rate chemistry model and an Arrhenius pyrolysis model are calibrated to strand burn rate data by modeling a quiescent environment using DNS. Subsequent DNS calculations are made where crossflow is induced from $M = 0.0$ to $M = 0.8$. The increased regression rate with increasing M and the resulting flame structure are studied.

The results of the DNS analysis are incorporated into a three-dimensional interior ballistics code and used to predict the chamber pressure of a motor known to have extensive erosive burning. The purpose of this step is to evaluate the magnitude of the DNS-predicted rate increase due to crossflow as compared to the base burn rate. The DNS results are incorporated in the ballistics code in the following way:

$$r_e = r(r|_M / r_o)|_{\mathrm{DNS}} \tag{1}$$

The local burn rate ($r =$ local burn rate, $r_e =$ erosive burn rate) is calculated using cP^n and then adjusted upward based on the local M and the ratio predicted through the DNS analysis. Finally, a simplified heat-transfer-based model using an infinite-rate chemistry model is proposed and similarly evaluated.

II. Governing Equations and Boundary Conditions

A. Overview of Direct Numerical Simulation Code

In DNS analysis, all fluid and chemical structures are resolved down to the resolution of the grid; thus there is no need for the assumption of laminar or turbulent flow. However, grid resolution must be carefully considered. The conservation equations are solved directly with no need for subscale modeling of turbulence or mixing. A fully compressible two-dimensional finite differencing DNS code has been written based on an extended MacCormack scheme.[10] Grid stretching is utilized in the analyses by stretching away from the propellant surface in all directions to ensure high resolution in the regions of large gradients. Characteristic boundary conditions are applied at the inlets and outlets. Conduction in the solid propellant and the surface energy balance derivatives are calculated using high-order forward and backward schemes. Accuracy of the code is demonstrated by calculating Poiseuille flow in a channel.

B. Governing Equations

The governing equations that are solved in the DNS analysis of the erosive burning problem are the conservation of mass, momentum, and energy, as well as the ideal gas equation of state. With the inclusion of finite-rate chemistry, the conservation of species and the caloric equation of state are required. The conservation equations are listed below in order of the conservation of mass, momentum, energy ($E =$ total energy, $q =$ heat flux), the ideal gas equation of state ($R_u =$ universal gas constant), the conservation of species, and the caloric equation of state:

$$\partial_t \rho + \partial_i(\rho u_i) = 0, \qquad \partial_t(\rho u_i) + \partial_j(\rho u_i u_j) = -\partial_j p\delta_{ij} + \partial_j \tau_{ji}$$

$$\partial_t(\rho E) + \partial_i(\rho u_i E) = -\partial_i q_i - \partial_i(p u_i) + \partial_j(\tau_{ji} u_i)$$

$$p = \rho \frac{R_u}{\mathrm{MW}} T$$

$$\partial_t(\rho Y_m) + \partial_i[\rho Y_m u_i + \rho V_{i,m} Y_m] = \rho \dot{\omega}_m, \qquad m = 1, N$$

$$h_m = \Delta h^o_{f,m} + \int_{T_o}^{T} c_{p,m}(T)\,\mathrm{d}T \tag{2}$$

Thermochemical equilibrium calculations (NASA–Lewis code)[11] are made at the chamber conditions to find the viscosity (μ) and the Prandtl number (Pr). The conductivity is then calculated as

$$k_g = \mu C_p / Pr \tag{3}$$

where the gas specific heat (C_p) and molecular weights (MW) are also derived from the equilibrium calculations. All properties are calculated at the applied pressure boundary condition used in the DNS calculations.

C. Gas Phase Boundary Conditions

The computational domain considered is a portion of a two-dimensional channel with the burning propellant located at midcenter on the bottom wall. Following the work of Poinsot and Lele,[12] characteristic boundary conditions are prescribed at the domain's inlet and outlet. The solid bottom wall is treated as a no-slip surface, and the inlet and outlet are treated as nonreflecting, subsonic

boundaries. Since the propellant is assumed to be burning in fully developed turbulent flow, the prescribed inlet velocity profile enforces this condition. The inlet and walls are given an initial and constant chemical composition. The burning propellant is assumed to flux gas at a fixed chemical composition into the fluid computational domain.

The inlet fluid is assumed to be combustion products at a stagnation temperature (T_o) equal to the adiabatic flame temperature of the propellant. For each DNS calculation, the inlet freestream M_∞ is set; thus the freestream static temperature is calculated as

$$T_\infty = T_o \Big/ \left[1 + (\gamma - 1) M_\infty^2 \Big/ 2\right] \tag{4}$$

from which the freestream velocity is calculated as

$$U_\infty = M_\infty (\gamma R T_\infty)^{\frac{1}{2}} \tag{5}$$

The inlet velocity profile is based on fully developed turbulent channel flow with integral scale dimensions equal to the combustion chamber of the CKEM motor. The temperature profile is set based on the freestream velocity as

$$T_{ij} = T_o - \left(u_{ij}^2 + v_{ij}^2\right) \Big/ (2C_p) \tag{6}$$

where the i–j indices represent the local conditions at the inlet. The species inlet conditions are set to combustion products.

The outlet characteristic boundary condition is set as a nonreflecting subsonic outlet. This condition assumes constant pressure at infinity, with the pressure at the outlet adjusted by characteristic waves that are assumed to propagate from the constant pressure reservoir at infinity.

D. Thermal Transport Model

The rate at which the propellant burns is dependent on the energy balance at the solid-to-gas interface. Therefore, a thermal transport model that accurately establishes the temperature gradient at the surface, and thus the conduction into the solid, must be used. The energy equation for the solid reduces to

$$\rho_p C_s \partial_t T = \partial_i (k_s \partial_i T) \tag{7}$$

The conductivity (k_s), Ref. 13, specific heat (C_s), and density (ρ_p) of the solid propellant are assumed to be spatially invariant; thus the right-hand side of the equation coverts to a second derivative of temperature and is solved with a second-order central differencing scheme. The propellant density is the theoretical density for the subject propellant, and k_s and C_s are established by the mass ratio of AP to HTPB in the CKEM (compact kinetic energy missile)[‡] propellant, assuming that the minor ingredients are insignificant in mass fraction. During the solid propellants cure cycle, some shrinkage occurs, but this is assumed to have an insignificant effect on the theoretical value of ρ_p.

The regression of the propellant will impact the temperature gradient in the solid at the surface. To account for this without moving the solid grid, the thermal transport equations are adjusted to account for a moving reference frame, based on the local burn rate. The propellant is assumed to be fed into the combustion chamber at the rate the propellant is burning. The bottom of the propellant is held at ambient temperature, and the heat flux through the solid in the transverse direction is adjusted by interpolating the temperature solution in the solid upward by a distance of $r\,\mathrm{d}t$ during each time step. The energy equation is modified with the additional term $-(\partial_2 T)r$, so that it takes the form $\partial_t T = \alpha[\partial_{11} T + \partial_{22} T] - (\partial_2 T)r$, where $\alpha = k_s/\rho_p C_s$, and r is the local burn rate along the span of the propellant. The term accounts for the movement of cold propellant into the flame front. The local burn rate is used because the rate is not constant along the surface.

[‡]CKEM test data originated from the U.S. Army Aviation and Missile Command, Huntsville, AL, 2001, CKEM Program. Program Manager, George Snyder; Chief Engineer, Steve Casan; Propulsion Lead, Scott Michaels.

E. Gas–Solid Interface

In this analysis, radiation from the gas to the surface is not considered; thus the energy balance equation used is of the form

$$q_{\mathrm{gcon}} = q_{\mathrm{pcon}} - \boldsymbol{QM} \tag{8}$$

or in expanded form

$$k_g \partial_i T = k_s \partial_i T - \boldsymbol{QM} \tag{9}$$

where Q is the heat of pyrolysis. $\boldsymbol{M}$ is the mass flux from the burning propellant and can be related to the burn rate or pyrolysis rate as $\rho_p r$.

Cazan and Menon[13] and others[14] have incorporated a model of the form

$$r = A \exp(-E_a / R_u T_{\mathrm{surf}}) \tag{10}$$

to relate the surface pyrolysis rate to the propellant surface temperature. Using typical values for the activation energy (E_a) of AP and HTPB,[13] Eq. (10) can be used to predict the propellant burning rate if the surface temperature is known (T_{surf}). In this study, and in most conceivable situations, the base burning rate is measured and known as a function of pressure ($r = cP^n$), but the surface temperature and the preexponential factor are not.

To find the preexponential factor in Eq. (10), the pyrolysis equation can be forced to match a reference regression rate at some reference surface temperature. Using $r = cP^n$ as the reference regression rate, the constant A can be shown to equal

$$A = \frac{cP^n}{\exp\left(-E_a \Big/ R_u T_{\mathrm{surf}_o}\right)} \tag{11}$$

Substitution of Eq. (11) into Eq. (10) results in an equation that describes the regression of the propellant at surface temperatures above the reference condition:

$$r = cP^n \exp\left[(E_a/R_u)\left(1 \Big/ T_{\mathrm{surf}_o} - 1/T_{\mathrm{surf}}\right)\right] \tag{12}$$

Equation (11) and Eq. (12) are evaluated at the reference pressure. Equation (12) is incorporated into the surface energy balance equation, which is solved within each time step for the unique value of T_{surf}, given a value of T_{surfo} (surface temperature with no crossflow). The velocity of the gas injected from the burning propellant is calculated from a mass balance at the surface as

$$\rho_p r = \rho v_{\mathrm{norm}} \tag{13}$$

where v_{norm} is the gas velocity normal to the propellant surface. Although the normal gas velocity should be relative to the moving reference frame of the regressing propellant, the gas-to-solid density ratio is approximately 40:1; thus, the moving velocity of the solid surface is considered negligible when compared to the normal gas velocity.

III. Analysis of Finite-Rate Erosive Burning

The overall objective of this work is to use DNS to resolve the near wall region of a propellant burning in crossflow to study the mechanisms that produce the regression rate increase as a function of the crossflow-free stream M. The fundamental assumption is that closed-bomb-stand burn rate data are available for the subject propellant. An initial DNS calculation is made with no crossflow. The resulting propellant regression rate is calibrated to strand burn rate data by varying the heat of pyrolysis (Q) to produce a match. After the calibration step, the crossflow is increased in steps from $M = 0.0$ up to $M = 0.8$, and the resulting regression and flame structure are analyzed.

The governing equations in the fluid domain are solved using a MacCormack[15] scheme. The basic scheme is an explicit time marching scheme that produces second-order time and space accuracy. The time derivative at each time step is first calculated by calculating the spatial derivatives with a first-order forward scheme. The solution is temporarily advanced in time; the time derivatives are then

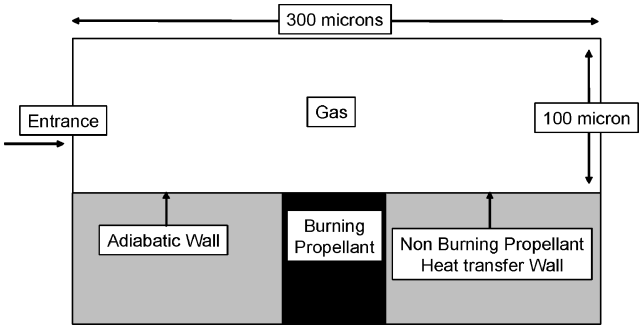

Fig. 2 Crossflow computational domain schematic.

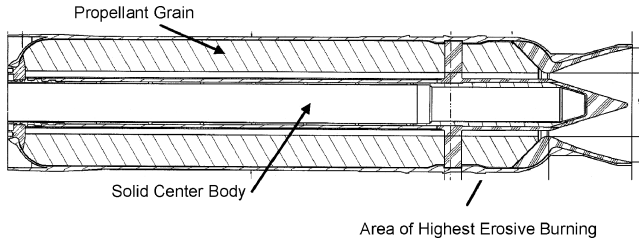

Fig. 3 CKEM rocket motor schematic.

recalculated based on the new values and a first-order backward scheme. The two time derivatives are averaged, and the solution is permanently advanced one time step. The scheme is extended to fourth-order spatial accuracy by replacing the first-order forward and backward schemes with second-order forward and backward schemes.[10]

The computational domain is considered to be a two-dimensional segment of a large two-dimensional channel having an integral scale based on the selected full-scale motor geometry. The domain dimensions are 0.1 mm in the normal direction and 0.3 mm in the streamwise direction. Grid size requirements are set so that flow structures on the Kolmogorov scale can be adequately resolved (typically 300×100 in the tangential and normal directions, respectively). This scale represents the smallest scale in the model; thus the grid dimensions are below those required to model the turbulent structures. Grid stretching in all directions away from the propellant ensures a grid of good aspect ratio and subdissipation scale size in the vicinity of the propellant, approaching 0.25 mm at the propellant surface. Figure 2 shows a schematic of the computational domain. As the gas enters the domain, it flows over an adiabatic wall before reaching the burning propellant. Upstream burning in a full-scale motor will influence the entrance conditions, depending on the location in the motor; thus all possibilities cannot be considered. However, the boundary layers are expected to develop rapidly due to the high mass injection rate of the burning propellant so that the choice of the entrance conditions is less critical.

All computations are run on Pentium-4 machines. The solutions are run until the time-averaged propellant surface temperature and/or the time-averaged regression rate converge, usually requiring approximately 120 h of CPU time.

A. Propellant Properties

The U.S. Army's CKEM rocket motor,[‡] shown in Fig. 3, contains a high-rate HTPB/AP propellant and has been statically tested in several configurations and is chosen as the test case.

Considerable strand burn rate data are available for this propellant. As the figure shows, the propellant grain is cast to the same diameter as the throat; thus the initial Ms in the flow field will approach $M = 1.0$ at the aft end of the motor. The advantage of this test case is that the motor has been tested with the same propellant in different configurations, and thus gives opportunity to test the universalism of the erosive burning results generated through DNS.

The CKEM strand burn rate data show that the propellant has a nominal burning rate of 5.25 cm/s at a pressure of 17.24 MPa. Thermochemical equilibrium analysis is used to calculate the adiabatic flame temperature (T_{ad}), Pr, and other relevant thermodynamic proprieties. Since HTPB and AP constitute approximately 95% of the total mass of the formulation, properties of the solid are calculated based solely on the ratios of these two ingredients. The physical properties of the solid propellant and the combustion gases are shown in Table 1.

Table 1 Physical properties of selected solid propellant and combustion gases

Physical properties	Values
Adiabatic flame temperature (T_{ab})	3024 K
Prandtl number (Pr)	0.58
Viscosity at T_{ab} (μ)	1×10^{-4} Pa-s
Solid propellant conductivity (k_s)	0.397 W/m-K
Solid density (ρ_p)	1744 kg/m^3
Solid specific heat (C_s)	1256 J/kg-K
Heat of pyrolysis (Q)	11.6×10^5 J/kg
Pyrolysis activation energy (E_a)	21.12 kcal/mol

B. Finite-Rate Chemistry Model

In the flame zone above the homogeneous solid propellant, several heat release regions exist at varying distances from the propellant surface. The most influential of these flames are the premixed exothermic decomposition of AP and the premixed flame of decomposed AP and binder gases. The heat feedback from these flames and from the freestream to the propellant surface determines the rate at which the propellant will pyrolyze.

The reaction rate of the AP decomposition is very fast[13] compared to the binder–APd reaction. The location of the flame will be determined from a balance between the species velocity originating from the propellant surface and the reaction rate of the decomposition process. Thus, the location of the APd flame is not expected to be influenced substantially by the addition of crossflow. However, because the reaction rate is temperature-dependent, a change in the temperature profile through the boundary layer as a result of crossflow will impact the reaction rate profile of the APd.

The premixed flame between the APd and the HTPB binder is influenced by the turbulent boundary layer in crossflow. As the crossflow increases, and the turbulent intensity increases, the effective conductivity increases. In addition, the boundary layer thickness is reduced. The additional heating from the freestream increases the reaction rate and reduces the APd and binder flame thickness.

The purpose of this study is to investigate the magnitude of the influence crossflow has on these mechanisms. Based on other studies,[8] the chemistry time scales are expected to be much smaller than the flow time scales, and thus will show negligible correlation to the freestream crossflow velocity.

All species are assumed to have the same mass diffusivities, found from the Lewis number ($Le = \alpha/D$, where α is the thermal diffusivity and D is the mass diffusivity). The assumed finite-rate model gas properties are MW = 27.3 kg/kmol, $C_p = 1800.2$ J/kg, $Pr = 0.6$, and $Le = 1.0$.

The four chemical species considered in the analysis are AP gas, APd gas, binder gas, and combustion products. Two chemical equations, shown in Eq. (14), are required to relate these species in the chemical model:

$$\mathrm{AP} \rightarrow \mathrm{APd}, \qquad \beta\mathrm{APd} + \mathrm{Binder}_{\mathrm{Gas}} \rightarrow \mathrm{Combustion\ Products} \tag{14}$$

where β is the mass stoichiometric coefficient. Two global reaction rate equations[13] are required to complete the chemical model and

[‡]CKEM test data originated from the U.S. Army Aviation and Missile Command, Huntsville, AL, 2001, CKEM Program. Program Manager, George Snyder; Chief Engineer, Steve Casan; Propulsion Lead, Scott Michaels.

are shown in Eq. (15):

$$R_1 = D_1 P_o^{n_1} [\mathrm{AP}] \exp(-E_1/R_u T)$$

$$R_2 = D_2 P_o^{n_2} [\mathrm{APd}][\mathrm{Binder_{Gas}}] \exp(-E_2/R_u T) \qquad (15)$$

where the [ ] quantities are the concentrations of the species, and D_i, n_i, and E_i have been taken from previous studies and represent experimental data. The law of mass action is used to complete the rate of production of the remaining two species. The finite-rate chemistry model input is $D_1 = 2.234 \times 10^7$, $D_2 = 1.105 \times 10^7$, $E_1/R_u = 8000$ K, $E_2/R_u = 11{,}000$ K, $n_1 = n_2 = 1.0$, and $\beta = 8.1$ (units for D are atm for P, and kmol/m^3 for [ ]).

C. Model Definition and Boundary Conditions

The mass fractions of all species are set at the boundaries, as well as initially throughout the computational domain. Heats of formation (h_f^o) for all species are specified so that the split of chemical energy to sensible energy may be tracked. Species diffusion velocities are calculated and thus require the input of mass diffusivities.

The total heat release from all reactions is set equal to the adiabatic heat release of the propellant as calculated by thermochemical equilibrium. Because only two reactions are considered, the heat release from the APd flame and the APd–HTPB flame must be equal to the total heat release from the propellant. For an adiabatic system, the total enthalpy of a reaction is constant, only the distribution between sensible (h_s) and chemical enthalpy changes as shown in Eq. (16):

$$\left(h_f^o + h_s\right)_{\mathrm{AP}} = \left(h_f^o + h_s\right)_{\mathrm{APd}}$$

$$\eta\left(h_f^o + h_s\right)_{\mathrm{APd}} + (1-\eta)\left(h_f^o + h_s\right)_{\mathrm{HTPB}} = \left(h_f^o + h_s\right)_{\mathrm{Products}} \qquad (16)$$

where η represents the mass fraction of the APd in the APd–HTPB reaction. A thermochemical equilibrium calculation is run to find the adiabatic heat release, or sensible enthalpy of the APd reaction. From this, and the heat of formation of the AP, the heat of formation of the APd is calculated. The heat of formation of the final combustion products is then found from Eq. (16) by setting h_s of the products to the thermochemical calculation value, and h_s of the HTPB to the tabulated value. Table 2 shows the results.

D. Model Calibration Procedure

The initial step in developing the finite-rate chemistry model is to calibrate the analysis to strand burner data. Although several suitable variables could be used for calibration, only one data point is available, namely the measured burn rate. Thus, only one variable can be used for calibration. The remaining physical properties must be accepted from the literature. In the calibration step, no crossflow is induced, with boundary conditions set so that the domain pressure will converge to the desired value at infinity. Equation (12) is used to describe the pyrolysis rate as a function of temperature and pressure. A reference burn rate and reference temperature of 0.17 cm/s and 835 K, respectively, are chosen from the literature[14] for a similarly formulated propellant. Using these reference values, Eq. (12) is forced to match strand burn rate data with no crossflow. The solution is allowed to converge to the regression rate and surface temperature that produces an energy balance at the surface. If the calculated regression rate does not match strand data, the heat of pyrolysis is adjusted and the procedure repeated. Once the model is calibrated, crossflow is induced while the heat of pyrolysis is held constant. The reference conditions in Eq. (12) are changed to the surface temperature found in the no-crossflow condition using the strand burn rate as the reference rate. Thus, the crossflow conditions are perturbations from the calibrated no-crossflow conditions.

Table 2 Heats of formation of considered species

Ammonium perchlorate, h_f^o	−2520.51 kJ/kg
Ammonium perchlorate, h_s	0.0 (at Ref. Condition of 298. K)
Ammonium perchlorate decomposed, h_f^o	−4092.68 kJ/kg
Ammonium perchlorate decomposed, h_s	1572.17 kJ/kg
HTPB, h_f^o	−1001.5 kJ/kg
HTPB, h_s	0.0 (at Ref. Condition of 298. K)
Combustion products, h_f^o	−7213.19 kJ/kg
Combustion products, h_s	5032.4 kJ/kg
η	0.8901

The selection of the reference temperature and reference rate is not viewed as highly critical in this analysis, but serves as a reasonable starting point for the calibration step. Minor ingredients can produce drastic changes in the regression rate of a propellant. The calibration step is critical to establish the proper base burning rate for the particular propellant in the analysis under the no-crossflow condition. Several other variables exist in the model that are candidates for use in the calibration step. Because the regression rate is ultimately determined by the energy balance at the solid–gas interface, the most likely candidates are the solid conductivity, the gas conductivity, and the heat of pyrolysis. The solid conductivity is not significantly altered by minor ingredients, is easily measured, and can be selected from data on any propellant with similar mass ratios of AP and HTPB. Both the gas conductivity and the heat of pyrolysis can be affected by minor ingredients and have more uncertainty in their true values. Because altering the gas conductivity will either change the Pr, or change the gas viscosity (holding the Pr constant), the heat of pyrolysis is chosen as the calibration variable. The calibration steps in the analysis produce heats of pyrolysis that are very reasonable, and are in the range of values published for an AP/HTPB propellant.

E. Finite-Rate Model Results

The results of the finite-rate analysis are shown in Table 3, showing also the calculated rates normalized by the $M = 0.0$ values.

The calibration run for $M = 0.0$ results in a surface temperature of 1143.8 K. The normalized rate increase ranges from 2.8% at $M = 0.1$ up to 22% at a freestream M of $M = 0.8$. The normalized surface temperature increases associated with the predicted rates range from 0.28% at $M = 0.1$ up to 2.0% at $M = 0.8$. The results show that the surface temperature increase is small compared to the rate increase, due to the high activation energy in the pyrolysis law.

Figure 4 shows a comparison of the near-wall temperature gradients in the normal direction at the midpoint of the burning propellant.

The gradients are as expected, showing an increase near the wall as the freestream M increases. Figure 5 shows these gradients out

Table 3 Finite-rate model results

Mach number	Rate (cm/s)	Surface temperature (K)	Rate ratio (r/r_o)
0.0	5.295	1143.8	1.0
0.1	5.444	1147.02	1.0028
0.5	6.018	1158.89	1.0132
0.8	6.453	1167.22	1.0205

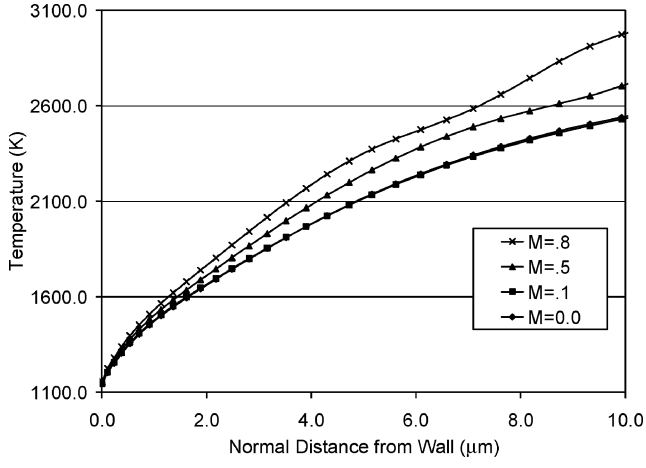

Fig. 4 Near-wall temperature profile.

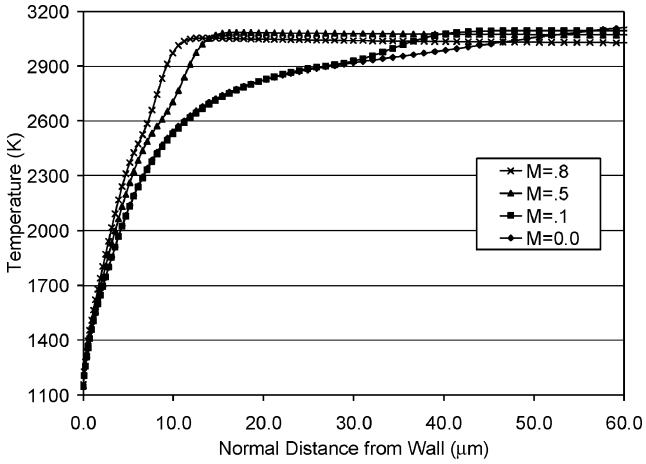

Fig. 5 Temperature profiles out to thermal boundary layer edge.

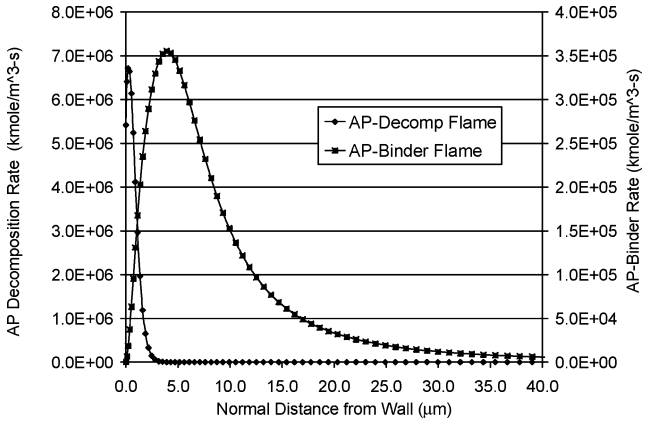

Fig. 6 Comparison of the AP decomposition and APd–binder flame thicknesses for $M = 0.0$.

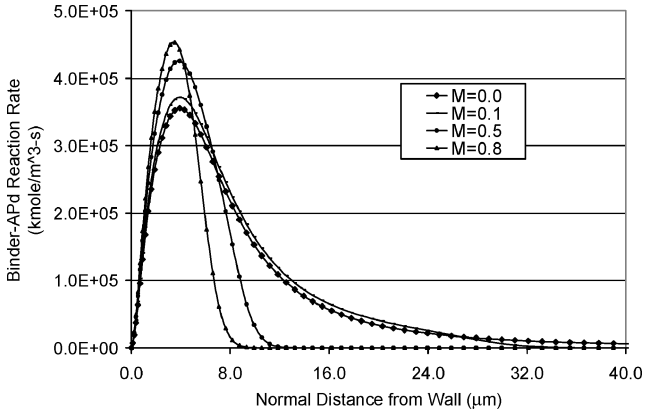

Fig. 7 APd–binder flame thickness comparison for various freestream Mach numbers.

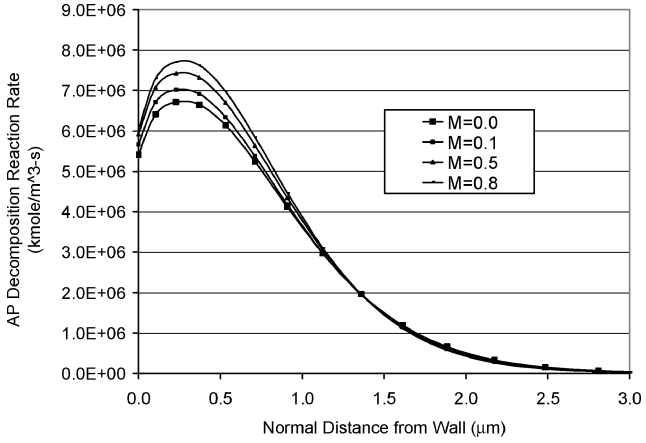

Fig. 8 AP decomposition flame thickness comparison for various freestream Mach numbers.

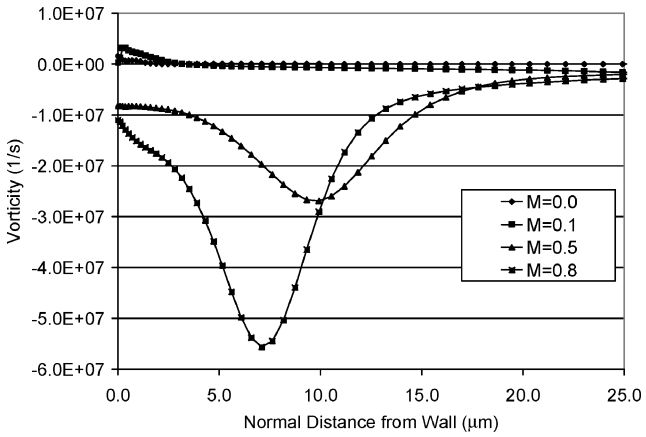

Fig. 9 Near-wall vorticity for various freestream Mach numbers.

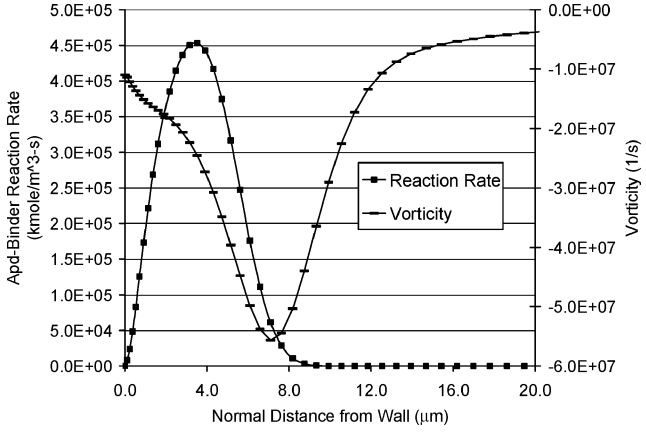

Fig. 10 APd–binder flame and vorticity for $M = 0.8$.

to the extent of the thermal boundary layers. The increase in heat transfer to the wall as the M increases is evident in the curves. The curve for $M = 0.8$ shows considerable deviation from the isentropic and adiabatic entrance profile.

The flame thicknesses for the AP decomposition flame and the APd–binder flame are shown in Fig. 6 for the $M = 0.0$ calibration analysis. The figure shows a very thin decomposition flame which approaches the resolution limits of the model. However, several grid points exist between the wall and the maximum-reaction-rate region. The flame is on the order of 3 μm thick. The APd–binder premixed flame is highly resolved and approaches 40 μm in thickness.

Figures 7 and 8 show the effect of increasing the crossflow velocity on the flame thicknesses. Of great interest is that as M increases, the flame thicknesses decrease, but the relative distance of the maximum reaction rate from the wall changes very little. Of note in Fig. 8 is that the increase in M has only a slight effect on the AP decomposition flame thickness. This slight thickness decrease is attributed to the increase in temperature, due to the compressed boundary layer, that produces a reaction rate increase near the wall.

Figure 9 shows that as the M increases, the near-wall vorticity increases, with the maximum point moving close to the outer edge of the diffusion flame.

This is shown more clearly in Fig. 10, where the APd–binder flame is plotted with the vorticity for a freestream M of 0.8. The source of the vorticity is shown in Fig. 11, where the tangential velocity profiles are plotted. The plot shows considerable lifting of the

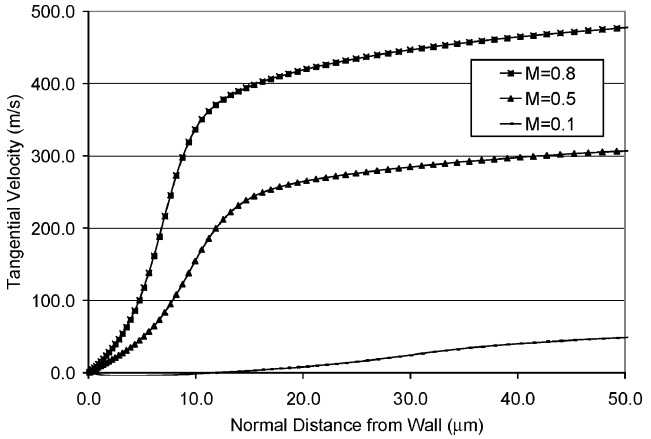

Fig. 11 Near-wall tangential velocity profiles.

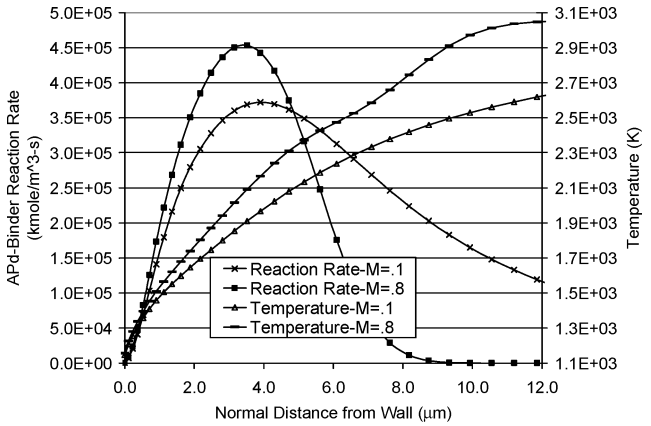

Fig. 12 Comparison of reaction rate gradients to thermal gradients.

velocity boundary layer due to the side injection of the combustion gases, thus creating large tangential velocity gradients in the normal direction. The net result appears to be an increase in the reaction rate of the decomposed AP and binder gases, with a resulting decrease in the flame thickness. The stand-off distance of the point of maximum heat release of the decomposition flame changes little.

The starting location of the premixed flame is dependent on the precursor AP decomposition flame. Because there is little change in the decomposition flame, the start of the APd and binder flame remains relatively stationary. Thus the results show that turbulence reduces the APd and binder flame thickness, but does not significantly change the stand-off distance of the location of the maximum heat release zone.

Figure 12 shows that the thermal gradient is fairly constant from the edge of the thermal boundary down to the wall. No discontinuities are shown in the thermal profile as it passes through the APd and binder flame. Because the regression rate is determined by the energy balance at the solid–gas interface, the conclusion is that the controlling parameters in the heat flux to the surface are the surface temperature, and the free stream conditions. Although the temperature gradient at the wall varies with M, it appears to be weakly influenced by the flame zone.

F. Reduced Base Burn Rate Analysis

The literature shows that as the base burning rate is lowered, the percent increase in rate due to crossflow increases. Thus, low-burning-rate propellants are more affected by crossflow. This supports the conclusion in the previous section that the flowfield dominates the regression rate. If the heat flux into the propellant surface is largely dictated by the crossflow conditions, then when crossflow is introduced, and the heating rate increases, the surplus energy that is conducted to the surface will be predominantly a function of the freestream M, and not the base burning rate of the

Table 4 Results of the low rate analysis

	Base rate (cm/s)	Rate at $M = 0.8$ (cm/s)	Ratio (r/r_o)	Surface temperature (K) at $M = 0.8$
Low rate	2.698	4.128	1.53	1111.72
High rate	5.295	6.453	1.21	1167.22

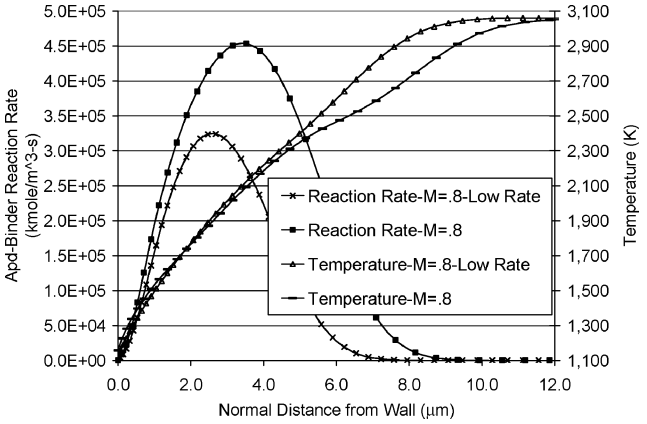

Fig. 13 Comparison of thermal gradients through the APd–binder flame for a high-rate and low-rate propellant.

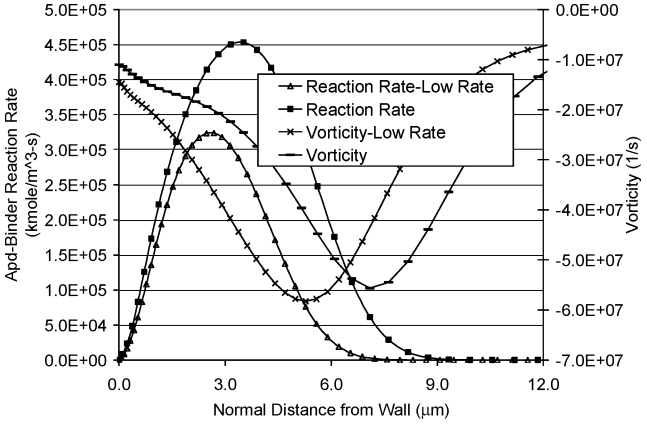

Fig. 14 Comparison of vorticity through the APd–binder flame for a high-rate and low-rate propellant.

propellant. The propellant's regression rate must rise to meet the heating rate of the freestream and balance the surplus energy at the surface. Thus, if the required regression is determined by the freestream, then the percent increase with M will increase when compared to a lower base rate.

To investigate this, a second analysis is run where the base rate (no crossflow) is artificially reduced by approximately 50% by increasing the heat of pyrolysis. All other boundary conditions remain the same (i.e., pressure). This model is then subjected to crossflow for a freestream condition of $M = 0.8$. Shown in Table 4 are the results of the analysis. The erosive burning rate increases by 53% in the low-rate case, as compared to 21% in the high-rate case.

Figure 13 shows a comparison of the thermal gradients for the high- and low-rate propellants through the APd–binder flame. The high-rate curve shows the edge of the thermal boundary layer to be further from the wall, representing more heat loss to the wall. However, the curves converge prior to either APd and binder flame, and continue to the wall at approximately the same slope. Figure 14 shows that the point of maximum vorticity moves closer to the wall with the lower burn rate. This is to be expected because the lower injection velocity in the low-rate case will not displace the velocity boundary layer as much. Of note is that the AP and binder flame thickness is reduced in the low-rate case in proportion to the movement of the maximum vorticity location.

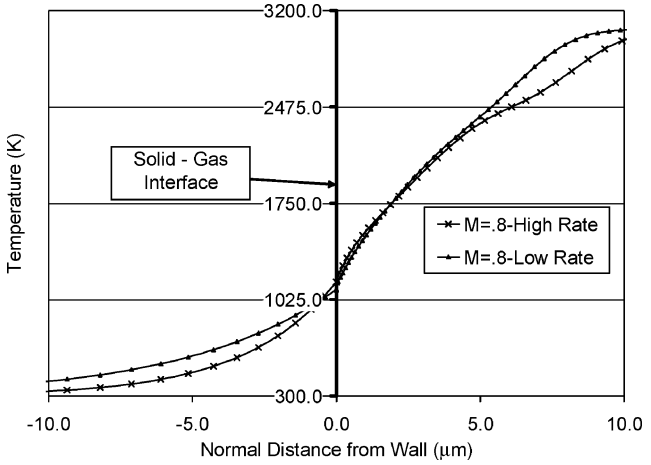

Fig. 15 Comparison of thermal gradients at the solid–gas interface for high-rate and low-rate propellants.

Figure 15 shows a comparison of the thermal gradients at the solid–gas interface between the two cases. On the gas side, the slopes converge from approximately 5 μm down to the wall. The solid side shows a distinct difference in slope. The low-rate propellant allows the surface heat to penetrate further into the solid resulting in a shallower slope at the surface and less heat loss from the freestream. The high regression rate keeps the thermal gradient high on the solid side, which results in more heat loss from the freestream.

G. Infinite-Rate Chemistry Model

To isolate the influence of the flowfield on erosive burning from chemistry, a second analysis is performed using a simplified infinite-rate chemistry model. Because of this assumption, this approach can be considered a heat-transfer-based model. As such, the calibration process ($M = 0.0$) is to match the heat transfer into the solid from the freestream that produces a regression rate matching strand burn rate data. The primary assumption in this approach is that the heat release zone is fixed at the propellant surface, and the mass flux from the surface is of combustion products only. The total energy (internal plus kinetic) of the combustion gases is set to the calculated total energy of the adiabatic flame. The objective of this study is to examine the increased rate of pyrolysis of the propellant as crossflow is induced for a range of freestream Ms due to heat transfer from the freestream alone.

H. Constant Surface Temperature Analysis

In the finite-rate analysis, the results showed that the increase in pyrolysis rate with M far exceeded the increase in surface temperature. Referring to Table 3, an increase in pyrolysis rate of 21% at a free-stream M of $M = 0.8$ resulted in a surface temperature increase of only 2.%. The high activation energy in the Arrhenius pyrolysis law leads to this relationship between the pyrolysis rate and the surface temperature. Given the very small temperature rise with pyrolysis rate, the pyrolysis rate law is eliminated from the infinite-rate chemistry model. The regression rate is then calculated directly from an energy balance at the surface, while the surface temperature is held constant. Calibration of the model is done by varying the heat of pyrolysis, as in the finite-rate analysis. The propellant surface temperature is fixed at a value of 1143 K, which matches that which was produced in the finite-rate analysis. The calibration analysis ensures that the heat transfer condition at the surface for no crossflow produces the strand burn rate.

Applying the infinite-rate model at the surface will generate a temperature jump between the first and second grid cells due to the enthalpy discontinuity. To account for this jump, the gas-side temperature gradient used in the surface energy balance and regression rate calculation is calculated with high-order schemes to include grid points beyond the jump region.

Using the assumed surface temperature and heat of pyrolysis from the zero crossflow case, DNS runs are conducted at freestream Ms of $M = 0.1$, and 0.8. The DNS calculations are run until a steady, time-averaged regression rate is achieved. The results of the infinite-rate analysis are plotted in the form (r/r_o) versus M and shown in Fig. 16.

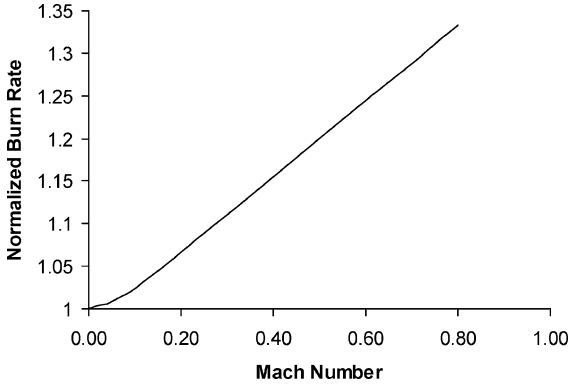

Fig. 16 Normalized burn rate versus Mach number for infinite-rate model.

IV. Application of Direct Numerical Simulation Results

Of primary interest in the study of erosive burning is the development and improvement of design and analysis tools for solid rocket motors. Several erosive burning models have been developed and implemented in interior ballistics codes with varying success. Most of these models are of the form of the Lenoir–Robillard model,[16] which is perhaps the most widely used in industry:

$$r_e = r + (\alpha G^{0.8}/D^{0.2}) \exp(-\beta \rho_p r/G) \tag{17}$$

Most models are of a similar form, showing the total burn rate as a summation of the base burn rate (r) and a term containing empirical constants (α, β), mass flux (G), and length scales (D), which account for crossflow induced burning.

To test the validity of the DNS results presented, a simplified erosive burning model is added to an interior ballistics code and used to predict the chamber pressure of an existing full-scale rocket motor. The form of the model is a simple amplification of the local base burn rate by the ratio of the DNS predicted rate at a given M to the DNS predicted base rate, as shown in Eq. (1).

A. Interior Ballistics Code Description

The interior ballistics code used in this study, called 3DGE (three-dimensional grain evaluation), was developed by the Stone Engineering Company[17] for the United States Army Aviation and Missile Command. The objective of the code development was to provide a means of accurately predicting the rocket motor performance parameters of high-burn-rate, high-internal-M, short-burning motors. The code is unique in that it begins with a three-dimensional finite element grid representation of the propellant geometry, which is regressed locally based on the local burning rate. An extensive library of burning rate models is available, including the Lenoir–Robillard model. The code was first developed in 1995 and has been used extensively to predict or simulate the ballistics of several U.S. Army solid rocket motors.

The governing equations for the 3DGE ballistics code represent a time-accurate, compressible, inviscid, and one-dimensional flowfield. Infinite-rate chemistry and a single-species working fluid are assumed. The governing equations are solved using a Lax–Wendroff scheme,[18] which gives second-order accuracy in time and space.

B. Solution Methodology

An interior ballistics model of the CKEM-4 rocket motor is constructed using 3DGE. The configuration of this motor is shown in Fig. 3. The CKEM motor is selected as the test case due to the availability of strand burn rate and full-scale static test data. As the figure shows, the motor is annular and has an initial port-to-throat

ratio equal to 1; thus high Ms are generated in the firing and produce characteristic erosive burning features in the test data. The pressure boundary condition in the DNS analysis is 17.24 MPa (2500 psi), which is the average chamber pressure of the CKEM motor.

C. Ballistics Analysis Using the Finite-Rate Direct Numerical Simulation Model

Figure 17 shows the results of the interior ballistics analysis compared to the CKEM-4 static test data. The model shows a reasonable match on the start-up transient. During this part of the motor operation, the internal Ms will be the highest. However, the plot shows that the predicted tail-off of the finite-rate model is too steep in slope. The shallower tail-off that is seen in the test data occurs when longitudinal propellant slivers are created in a motor due to burn rate gradients in the axial direction.

To simulate this, the erosive burning model must correctly predict the erosive burning level versus M. The steep tail-off and the slight underprediction of the start-up transient indicate that the erosive burning model is underpredicting the erosive rate versus M. However, the match between the test data and the simulation is very good in light of the fact that the DNS model was applied to strand burn rate data directly and then used to predict the motor pressure. Refer to Fig. 1 to see the prediction of the motor pressure using strand data alone. Although many assumptions are made in the analysis, one source of error is that the DNS model is generated for one base rate taken at the average motor pressure. As shown in the previous section, the relationship between the erosive amplification factor and base burn rate is not constant. In addition, in the finite-rate model three temperature rate equations are used, where the temperature dependency of each must be assumed. An example is the temperature dependency of the pyrolysis equation, which is not calibrated in the DNS analysis, but is taken from the literature.

The local burning rates as a function of axial distance from the head end of the motor, as calculated in the interior ballistics analysis, are shown in Fig. 18 for a slice in time shortly after ignition. The plot shows that the largest percent increase occurs at the aft end, as expected, because the aft has the highest M. However, the highest overall rate occurs at approximately $\frac{2}{3}$ from the head end, where the local pressure and local M combine for the largest total rate.

D. Ballistic Analysis Using the Infinite-Rate Direct Numerical Simulation Model

The infinite-rate DNS results are curve-fit and incorporated into the 3DGE internal ballistics code as in the finite-rate analysis. The resulting head-end pressure prediction shows excellent agreement and is also shown in Fig. 17.

The infinite-rate model shows excellent results in light of the assumption of constant surface temperature in the DNS simulation. In fact, in this case the infinite-rate model matches the test data slightly better than the finite-rate model. The infinite-rate model produces a higher erosion scale factor at $M = 0.8$ than does the finite-rate model, which accounts for the better match at the start-up. One explanation of the better match of the infinite-rate model is that it does not include the pyrolysis law used in the finite-rate analysis. The primary difference between the infinite-rate model and the finite-rate model is the treatment of the combustion heat release. Treatment of the flowfield is consistent between the two approaches. The similarity in the results emphasis the conclusion that combustion chemistry is not the dominate mechanism in erosive burning.

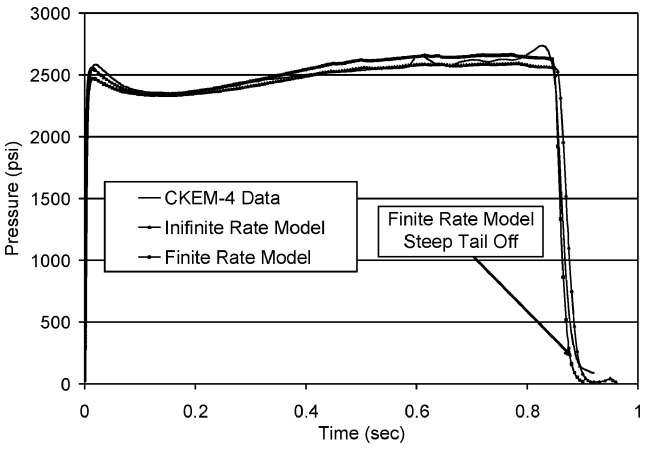

Fig. 17 Interior ballistics results with finite- and infinite-rate models.

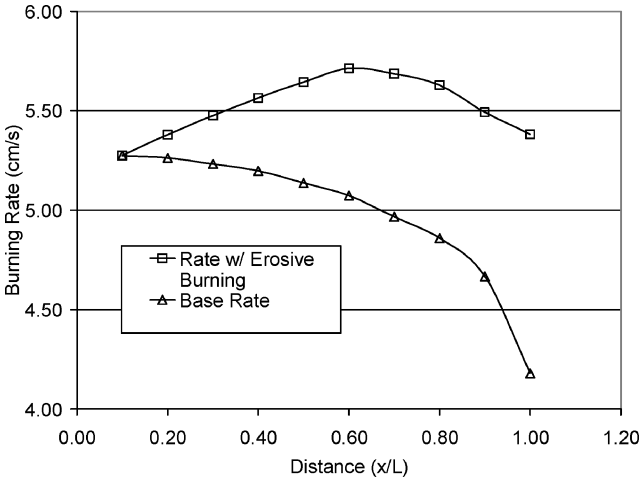

Fig. 18 Erosive burning rate compared to the base rate.

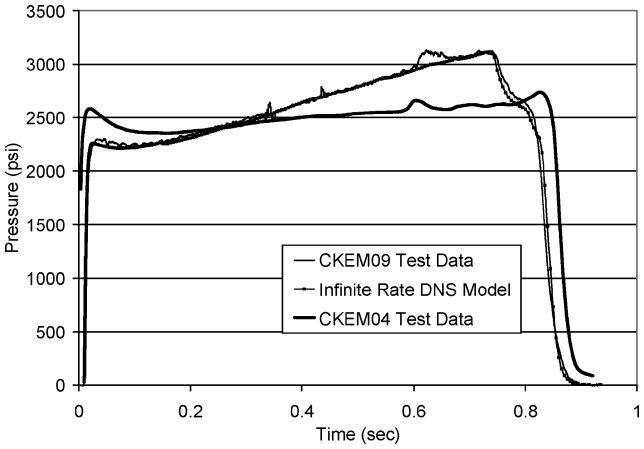

Fig. 19 Ballistics analysis of CKEM-9 using direct numerical simulation model.

E. Universality of the Infinite-Rate Chemistry Model

Typically in a motor design process, the propellant will be selected or developed, and then will experience few significant formulation changes there after. The results generated in both the finite-rate and infinite-rate models are based mainly on propellant properties. The only link to motor geometry is through the application of the turbulent velocity profile at the entrance, and the pressure boundary condition. Given this, the models should perform reasonably well when applied to other geometries that do not produce chamber pressures far from the assumed values in the DNS analyses.

Test data for several other CKEM configurations exist that contain the same propellant as the CKEM-4, but with slightly different propellant geometry and/or throat erosion histories. The net result of these differences is a modification of the average internal pressure, Ms, flowfield, and induced erosive burning.

The infinite-rate DNS model used to predict the performance of the CKEM-4 motor is again used to predict the performance of the CKEM-9 motor. The model is implemented in the ballistics code in the same way as in the previous analysis, as is shown in Eq. (1). Figure 19 shows a comparison of the predicted results of CKEM-9

to the static test data. Also shown in the figure are the test data of the CKEM-4.

A comparison of the test data between CKEM-4 and CKEM-9 show a noticeable difference in the pressure peaks that occur shortly after ignition. Typically, the magnitude of these pressure peaks is indicative of the amount of erosive burning present in a motor. (Other causes for initial pressure peaks may include nozzle closure and robust igniter.) In addition, the average operating pressures of the two designs are different. Thus, the two designs represent different test conditions for the DNS model. As the figure shows, the model has performed as well in the second case as in the first, indicating that the DNS model is not strongly dependent on the full-scale geometry. These results are reasonable because the only connection between the DNS calculations and the full-scale geometry is in establishing the integral scales for the turbulent velocity profile boundary condition at the entrance.

V. Conclusions

The primary objective of this work is to use DNS to resolve the near-wall region of an HTPB/AP solid propellant and study the mechanisms that produce an amplification of the burning rate when crossflow is introduced at the surface, as compared to the rate with no crossflow. Using a two-step finite-rate chemistry model calibrated to strand burn rate data, the APd–binder gas flame thickness is shown to reduce due to enhanced heating as near-wall vorticity increases with crossflow. The results also show that the stand-off-distance of this flame varies little with crossflow. Plots of the temperature gradients from the thermal boundary layer edge down to the wall show little variation as the curves pass through the flames, but show considerable dependency on the freestream condition. A comparison of the temperature slopes near the wall for a high-rate propellant and a low-rate propellant burning in identical freestream conditions show similarity, although the mass injection rate and flame structure are dissimilar. Finally, the comparison of the results of an infinite-rate model to the finite-rate model show excellent agreement in the erosive amplification factor as a function of M. In both models, the flowfield is equally resolved, with the only difference being the treatment of the heat release mechanism.

Using a simplified model, the results of both the finite-rate model and the infinite-rate model are incorporated into an interior ballistics code to demonstrate their validity by simulating the performance of a full-scale rocket motor, and comparing the results to static test data. Both models produce very good matches, when applied to strand burn rate data directly.

The conclusion from these results is that the burning rate amplification with crossflow that is seen in solid propellant combustion is dominated by the flowfield or freestream conditions, and loosely dependent on combustion chemistry. Treating the APd–binder flame as premixed will tend to hold the flame too close to the surface. However, even with this assumption, the chemistry is seen as secondary. Adding a mixing model for this flame may improve the fidelity of the model, but should not alter the conclusions. As such, a highly resolved heat-transfer-based model can be successfully developed, which eliminates the complexity of resolving the flame zone. However, the flow model must accurately treat the rotational flow that is generated in the near-wall region, which augments thermal transport properties and enhances wall heating. In addition, DNS is demonstrated to be an accurate and useful means to the design engineer for developing an erosive burning model, which is based on and calibrated to strand burn rate data. The demonstrated weak dependency on full-scale geometry is critical during a design phase where the configuration, but not the propellant, may experience much iteration.

References

[1]Graham, W. H., and Keller, K. D., "Burning Rate Studies with the Micro-Window-Bomb Strand Burner," *Technical Report s-214*, Rohm and Haas Company Redstone Research Laboratories, Feb. 1969.

[2]Sutton, George P., *Rocket Propulsion Elements*, Wiley, New York, 1967.

[3]Williams, F. A., *Combustion Theory*, Benjamin/Cummings, Menlo Park, CA, 1985.

[4]Razdan, M. K., and Kuo, K. K., "Erosive Burning Study of Composite Solid Propellants by Turbulent Boundary-Layer Approach," *AIAA Journal*, Vol. 17, No. 11, 1979, pp. 1225–1233.

[5]Gordon, J. C., Duterque, J., and Lengelle, G., "Erosive Burning in Solid Propellant Motors," *Journal of Propulsion and Power*, Vol. 9, No. 6, 1993, pp. 806–811.

[6]Bulgakov, Victor K., and Karpov, Alexander I., "Numerical Studies of Solid Propellant Erosive Burning," *Journal of Propulsion and Power*, Vol. 9, No. 6, 1993, pp. 812–818.

[7]King, Merrill K., "Erosive Burning of Solid Propellants," *Journal of Propulsion and Power*, Vol. 9, No. 6, 1993, pp. 785–805.

[8]Mukunda, H. S., and Paul, P. J., "Universal Behavior in Erosive Burning of Solid Propellants," *Combustion and Flame*, Vol. 109, April 1997, pp. 224–236.

[9]Apte, Sourabh, and Yang, Vigor., "Turbulent Flame Dynamics of Homogenous Solid Propellant in a Rocket Motor," *Proceedings of the Combustion Institute*, Vol. 28, 2000, pp. 903–910.

[10]Kennedy, C. A., and Carpenter, M. H., "Comparison of Several Numerical Methods for Simulation of Compressible Shear Layers," NASA Technical Paper 3438, Langley Research Center, Dec. 1997.

[11]Gordon, S., and McBride, B. J., "Computer Program for Calculation of Complex Chemical Equilibrium Compositions, Rocket Performance, Incident and Reflected Shocks, and Chapman–Jouguet Detonations," NASA SP 273, 1971.

[12]Poinsot, T. J., and Lele, S. K., "Boundary Conditions for Direct Simulations of Compressible Viscous Flows," *Journal of Computational Physics*, Vol. 101, No. 1, 1992, pp. 104–129.

[13]Cazan, R., and Menon, S., "Direct Numerical Simulation of Sandwich and Random-Packed Propellant Combustion," AIAA Paper 2003-5082, July 2003.

[14]A., Hegab, Jackson, T. L., Buckmaster, J., and Stewart, D. S., "Nonsteady Burning of Periodic Sandwich Propellants with Complete Coupling between the Solid and the Gas Phase," *Combustion and Flame*, Vol. 125, April 2001, pp. 1055–1070.

[15]MacCormack, R. W., "The Effect of Viscosity in Hypervelocity Impact Cratering," AIAA Paper 69-354, 1969.

[16]Lenoir, J. M., and Robillard, G., "A Mathematical Method to Predict the Erosive Burning Effect in Solid Rockets," *Proceedings of the 6th International Symposium on Combustion*, Reinhold, NY, 1957.

[17]McDonald, B. A., and Maykut, A. R., "A New Finite Element Based 1-D, Unsteady Finite Differencing Ballistics Code," CPIA Pub. 630, Vol. 1, Dec. 1995, pp. 97–106.

[18]Lax, P., and Wendroff, B., "Systems of Conservation Laws," *Communications Pure and Applied Mathematics*, Vol. 13, 1960, pp. 217–237.